INL/JOU-21-62333-Revision-0

Understanding fission gas bubble distribution, lanthanide transportation, and thermal conductivity degradation in neutron-irradiated a-U using machine learning

Lu Cai, Fidelma Giulia Di Lemma, Daniel J Murray, Cynthia A Adkins, Larry K Aagesen Jr, Michael T Benson, Luca Capriotti, Tiankai Yao, Min Xian, Fei Xu, Jeffrey J. Giglio

INL/JOU-21-62333-Revision-0

Understanding fission gas bubble distribution, lanthanide transportation, and thermal conductivity degradation in neutron-irradiated a-U using machine learning

Lu Cai, Fidelma Giulia Di Lemma, Daniel J Murray, Cynthia A Adkins, Larry K Aagesen Jr, Michael T Benson, Luca Capriotti, Tiankai Yao, Min Xian, Fei Xu, Jeffrey J. Giglio

February 2022

Idaho National Laboratory
Idaho Falls, Idaho 83415

http://www.inl.gov

Prepared for the
U.S. Department of Energy
Under DOE Idaho Operations Office
Contract DE-AC07-05ID14517

Understanding Fission Gas Bubble Distribution, Lanthanide Transportation, and Thermal Conductivity Degradation in Neutron-irradiated α-U Using Machine Learning

Lu Cai[1*]; Fei Xu[2,*]; Fidelma Dilemma[1]; Michael Benson[1]; Daniel J. Murray[1]; Cynthia A. Adkins[1]; Joshua J. Kane[1], Min Xian[3,#]; Luca Capriotti[1,#]; Tiankai Yao[1,#]

[*]Those authors contribute equally

[1] Idaho National Laboratory, Idaho Falls, ID, 834015, USA

[2] Grand View University, Des Moines, IA, 50316, USA

[3] University of Idaho, Idaho Falls, ID, 83406, USA

[#]Corresponding authors

Min Xian: Email: mxian@uidaho.edu

Luca Capriotti: Email: Luca.Capriotti@inl.gov

Tiankai Yao, Email: tiankai.yao@inl.gov

Abstract:

U-10Zr based metallic nuclear fuel is the leading candidate for next-generation sodium-cooled fast reactors in the United States. US research reactors have used and tested this fuel type since the 1960s and accumulated considerable experience and knowledge about the fuel performance. Most of knowledge, however, remains empirical. The lack of mechanistic understanding of fuel performance puts a large burden on proof through experimental verification for the qualification of U-10Zr fuel for commercial use. This paper proposes an image data-driven machine learning approach, coupled with domain knowledge provided by advanced post irradiation examination, to provide unprecedented quantified insights into the morphology, size, density and the connectivity of fission gas bubbles and its effect on the fission product transportation and thermal conductivity. Specifically, we developed a method to automatically detect, extract statistic, and classify ~19,000 fission gas bubbles into different categories, and quantitatively link the data to lanthanide transportation through connected bubbles and degradation of thermal conductivity along the radial temperature gradient in a neutron irradiated U-10Zr annular fuel. Results indicates the approach can be modified to study other irradiation effects, such as secondary phase redistribution and gaseous fuel swelling in other irradiated nuclear fuels.

Keywords:

Machine learning; Nuclear fuel; Fission gas bubble; Lanthanide migration; Thermal conductivity

1. Introduction

U-10wt.% Zr (U-10Zr) based metallic fuel is the leading candidate for next generation sodium cooled fast reactor due to low fabrication cost and capability to achieve a burnup of almost 20 at% [1]. Although U-10Zr fuel successfully powered or was tested in United State research reactors, such as Experimental Breeder Reactor Ⅱ (EBR-Ⅱ) and Fast Flux Test Facility (FFTF)[2], it has not been qualified for commercial use. Currently, Idaho National Laboratory (INL) has been the leading national laboratory for research and development (R&D) on metallic fuel in recent years spanning research on multiple metallic fuel forms[2] and post irradiation characterization[3,4]. Characterization capabilities ranging from sub-nanometer to micrometer, such as focused ion beam (FIB) sampling, transmission electron microscopy (TEM) characterization[3], and local thermal conductivity microscopy (TCM), have been utilized recently on U-10Zr fuel samples irradiated in EBR-II and FFTF to gain a better understanding of nuclear fuel microstructure and property evolution inside a reactor. The goal is to provide multiscale characterization of fuel microstructure and property measurements to support the development of fuel performance modeling tools, such as BISON[5], to facilitate fuel qualification by US Nuclear Regulatory Commission.

Under thermo-irradiation conditions, nuclear fuel microstructure is constantly changing with burnup. The thermal and mass transportation, particularly the movement of lanthanides under temperature gradient from fuel center to cladding inner surface, are key factors affecting fuel performance. The deposition of lanthanide at the cladding inner surface will potentially trigger a chemical reaction/interaction between nuclear fuel and cladding (FCCI)[6] to form Ce and Fe based intermetallic with low melting point. The eroded cladding due to FCCI is responsible for deteriorating the mechanical properties that could threaten fuel integrity and safety. How the lanthanides move through fuel and arrive at fuel cladding interface is therefore critically important for a mechanistic understanding of U-10Zr fuel performance. Post-irradiation examinations (PIE) on annular U-10Zr pin (~3.3 % burnup) show that the lanthanide particles/nodules deposit around the periphery of the pores in the outer fuel area[4]. Both PIE observation and existing theory[4] support the liquid-like transportation of lanthanides through interconnected bubbles from hot fuel center to cold cladding along the temperature gradient.

Unlike oxide nuclear fuel whose thermal conductivity relies on phonons, metallic fuel transports thermal energy via electrons. Therefore, the degradation of thermal conductivity for ceramic nuclear fuels due to scattering of phonons by irradiation induced defects[7], are typically absent for metallic fuel. Although irradiation defects are not a concern for the thermal conductivity of metallic fuel, fission gas bubbles, however, can lead to a 35% reduction of thermal conductivity for metallic fuel[8]. Fission gas bubbles show different size and distribution pattern along radial thermal gradient inside irradiated U-10Zr fuel. Bubbles in the cold rim zone close to cladding are large and of highly irregular shape, while they are primarily round and significantly smaller in the hot center zone[9]. The classic approach to study fission gas bubbles largely relies on image processing based on contrasts or manual selection and measurement of the bubbles of interest. Those techniques often carry human bias during measurement. Furthermore, advanced characterization method is producing large amount of data with bubble number beyond man's power to handle. Therefore, there is a strong need to develop a method that can accurately extract the fission gas bubble size, number density, and connectivity in an automated manner, and develop physical descriptors to capture their effect on lanthanide movement and fuel thermal conductivity without human bias.

In this paper, we provided a framework with four steps to extract statistical data for fission gas bubbles from large scanning electron microscopy images (7,000 × 7, 000 pixels). Traditional image processing methods were used to segment out the bubble regions and detect bubbles automatically in the first two steps. In the third step, we explored three bubble types: connected bubbles with lanthanides nodules; connected but empty bubbles; and isolated bubbles. Based on the observation of features for the three types of bubbles, we developed a machine learning model to distinguish the bubble types. In the model, we employed 18 features of bubbles, such as bubble’s mean intensity, size, intensity standard deviation, intensity histogram, intensity range and the shape convexity. A data driven machine learning approach, named as Decision Tree, was employed to generate a bubble classifier and validated against a manually annotated dataset with ~800 bubbles. Once trained, bubble detection and classification were applied across the entire fuel cross section to derive bubble statistic along radial temperature gradient.

2. The proposed method

2.1. Experimental data

Readers are advised to read our previous publications[3,4] for detailed advanced PIE study of this fuel cross section. Fig. 1 shows a gallery of bubbles inside the α-U region. Different bubble types are highlighted by red arrows in Fig. 1(b), bubbles in (Figs. 1(c), (e), and (h)) have lanthanide nodules on bubble inner surface. Fig. 1(f) is another area in α-U region with Fig.1(g) and 1(h) underscore the abundance of lanthanide inside the connected pores. The lanthanides transport through a liquid-like movement within connected bubbles[10]. Driven by temperature gradient, the lanthanides arrive at the fuel cladding interface with the help of liquid ***sodium (if present as the thermal bond between the fuel and cladding), and cesium***, a fission product with a melting point of 28 °C.

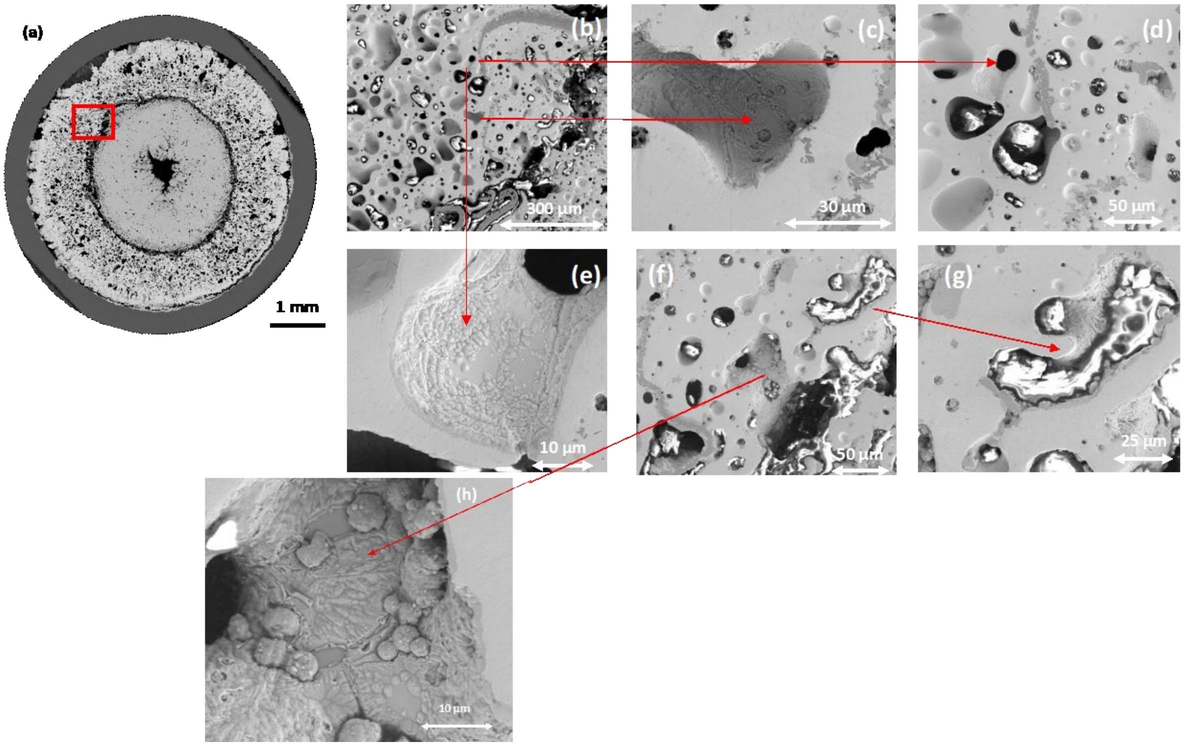

Fig. 1. The cross section of a U-10Zr irradiated to 3.4% fission per initial metal atom (FIMA) burnup (a) and different bubble types (b-h) in the outer ring zone of α-U. One bubble type is important for lanthanide transportation, showing residence of lanthanide nodules (h) inside.

FCCI occurs on the fuel cladding inner surface between lanthanides and Fe-based cladding. The source of lanthanides is the nuclear fission reaction, and the movement of lanthanides from hot fuel center to cold cladding is driven by the temperature gradient[11]. With high concentration of lanthanides at fuel rim, the interconnected pores are likely the major path for lanthanide transport as solid-state diffusion is too slow relative to the observed rate. The importance of interconnected bubbles to assist lanthanide movement has been shown by Fig. 1. To extract the bubble statistics, especially the type of bubbles and whether or not the bubbles have lanthanides in, is important for a better understanding of the roles played by bubbles on lanthanide movement and ultimately the FCCI.

The pipeline of the proposed method is shown in Fig.2. We process the U-10Zr microscopic images to segregate bubbles from the background (detailed in sections 2.2 and 2.3), and apply machine learning to classify the bubbles into different categories such as large/intermediate/small size and connected/isolated (as described in section 2.4). Lastly, we are using the data to analyze the implication on nuclear fuel performance.

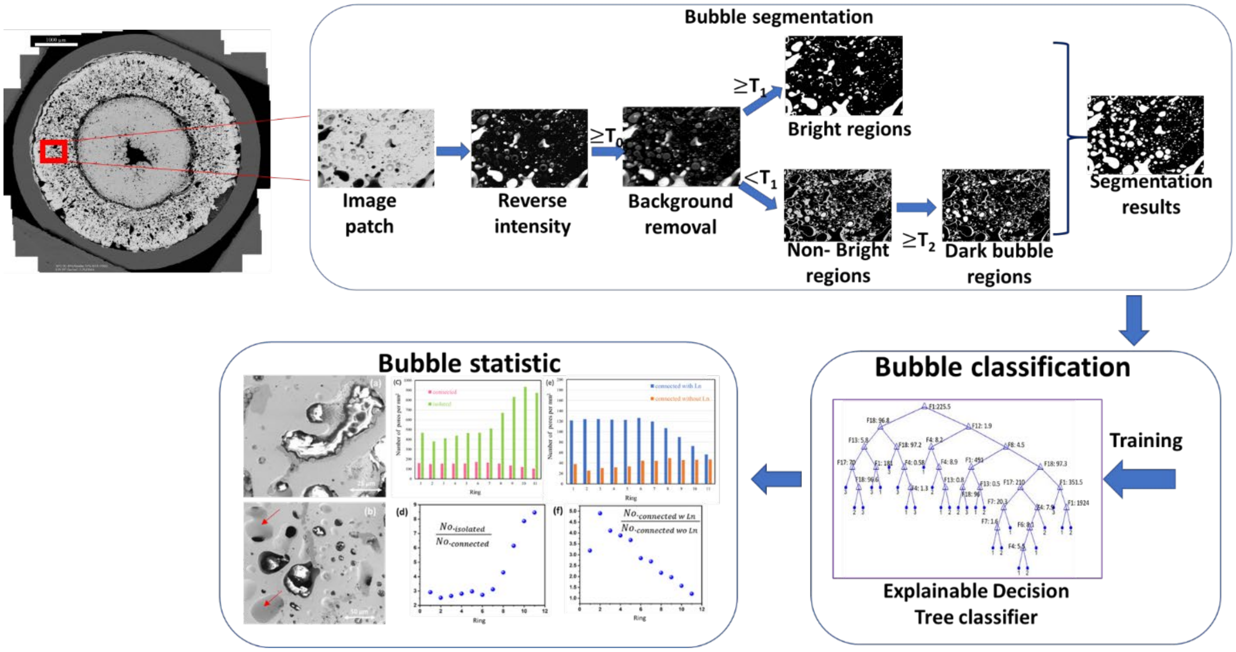

Fig. 2. Pipeline of the proposed approach.

2.2. Background removal

In SEM images, we define the non-bubble pixels as *background* and the bubble pixels as foreground which contained the *object* to be detected. As shown in Fig. 3(a), typically, the background appears brighter than the objects in the SEM images; and the bubbles have various shapes and sizes. We classify the bubbles into three categories: connected bubbles with fission product (white), connected empty bubbles (blue), and isolated bubbles (green), as shown in Fig. 3(*c*).

As shown in Fig. 3(a), the SEM original image is grayscale which means the value of each pixel position (i, j) in the image is between [0, 255]. The value for each pixel is named as intensity, and higher intensity appears brighter in the image. To make the bubbles more visible, firstly we reverse the image intensities by using the maximum intensity minus the current intensities. In the reversed image, the background appears darker than bubbles. Then the thresholding method[12] is applied to remove background regions. Thresholding will generate a binary image (Fig. 3(c)), i.e., if the image intensities are less than a threshold $\mathbf{T_0}$, the corresponding pixels assign 0s (background), otherwise assign 1s (bubble). One of the major challenges is to choose an appropriate threshold $\mathbf{T_0}$ to separate background and bubbles. A large threshold may lose some bubbles partially, while too small threshold will result in high false positives. The threshold $\mathbf{T_0}$ is chose by using the normalized histogram of pixels intensity values which is defined by

$$hist(k) = \frac{1}{N}\sum_{(i,j)} \delta(\lfloor \mathrm{I}(i,j)/d \rfloor, k)\,, k = 0, 1, \cdots, B-1 \tag{1}$$

$$\delta(\lfloor \mathrm{I}(i,j)/d \rfloor, k) = \begin{cases} 1, & if\ k = \left\lfloor \frac{\mathrm{I}(i,j)}{d} \right\rfloor \\ 0, & \text{otherwise} \end{cases} \tag{2}$$

where N is the number of image pixels; $\mathrm{I}(i, j)$ is the intensity of image pixel at location (i, j) whose value is in [0, 255]; $\lfloor \mathrm{I}(i,j)/d \rfloor$ denotes the floor division; d is the intensity interval which is set to 2; $\delta(\cdot)$ is an indicator function that accumulates pixels for each bin; and B is the number of bins of the histogram and is set as $\lfloor 255/d \rfloor + 1$. Therefore, the histogram defines the normalized frequencies ($\in[0,1]$) for all intensity values in each bin and is a simple and effective approach to describe image intensity distribution.

As shown in Fig. 3(d), there is a major peak between bins 0 to 20 which corresponds to the majority background pixels. Therefore, to remove the background pixels, the optimal threshold should be larger than the intensity of the peak. We set $\mathbf{T_0}$ to the intensity of the first peak. A peak is defined if its value is larger than the values of the three previous bins and the next three bins. Fig. 3(f) shows the background removal result of a sample image patch.

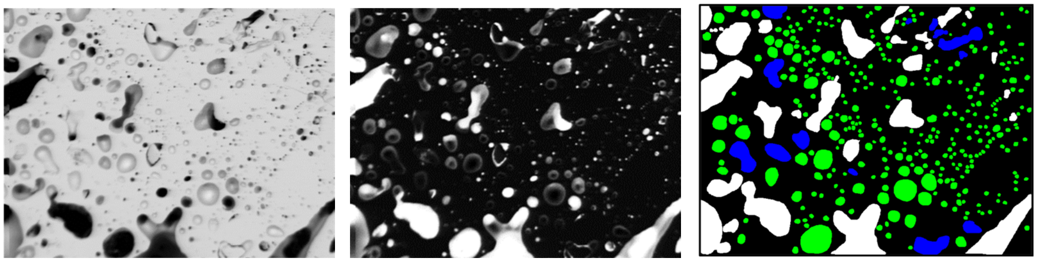

(a) Original image patch (b) Reversed intensities (c) Manually labeled

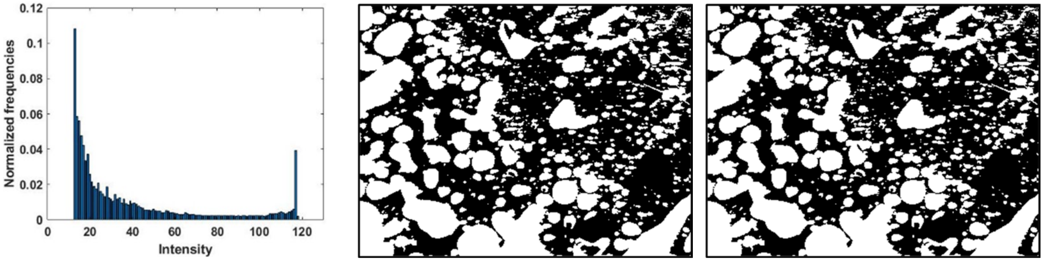

(d) Intensity histogram (e) Thresholding results (f) Background removal

Fig. 3. A sample image patch and background removal.

2.3. Bubble segmentation using automatic image thresholding

The background removal step excluded most background pixels as shown Fig. 3(f), bubble segmentation aims to extract fission gas bubbles from SEM images which will locate all bubbles and their boundaries in the coming section.

In the original SEM images (Fig. 3(a)), the gas bubbles have various sizes and shapes, and have both bright and black regions. Therefore, it is difficult to extract all bubbles using one single intensity threshold; and we proposed a double-threshold strategy to segment both dark and bright bubble regions automatically. The first threshold ($\mathbf{T_1}$) is applied to segment the bright regions, and a second threshold $\mathbf{T_2}$

is applied to extract dark bubble regions. $\mathbf{T_1}$ is chose as the first valley of the histogram of intensities of $\mathbf{I_1}$. A valley point has smaller value than its two neighboring bins. $\mathbf{T_1}$ separate pixels in $\mathbf{I_1}$ into two parts, bright regions (I_b) and non-bright regions (I_{nb}). The contrast of $\mathbf{I_{nb}}$ is stretched by linearly mapping its pixel intensities to [0, 255] before thresholding. $\mathbf{T_2}$ is chosen as the first valley after the second peak in the intensity histogram of the contrast enhanced I_{nb}, because the first peak is at bin 0 and refers to the large number of background pixels; and dark bubble regions correspond to intensities after the second peak.

Based on the observation (marked red arrows in Figs. 4(c) and 4(f)), a bubble could have both bright and dark regions, and these regions might be generated at different steps. Therefore, we develop a bubble size-aware strategy to combine the regions into one bubble. First, all dark bubble regions are put into four groups, large (> 2000 pixels), medium (500 - 2000 pixels), small (50 – 200 pixels) and extra small (10 - 50 pixels). Then morphological opening operations are applied to the large, medium and small groups to disconnect neighboring bubble regions. Finally, the logic union operation is applied to combine results from the above step and the $\mathbf{I_b}$.

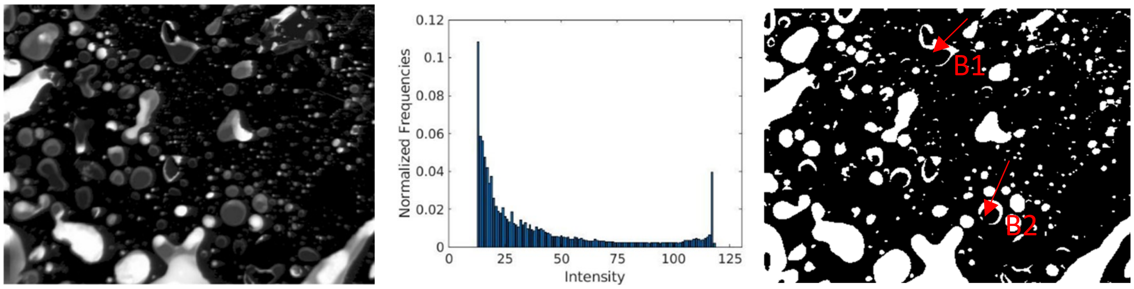

(a) I_1 (b) Intensity histogram (c) Bright bubble regions (I_b)

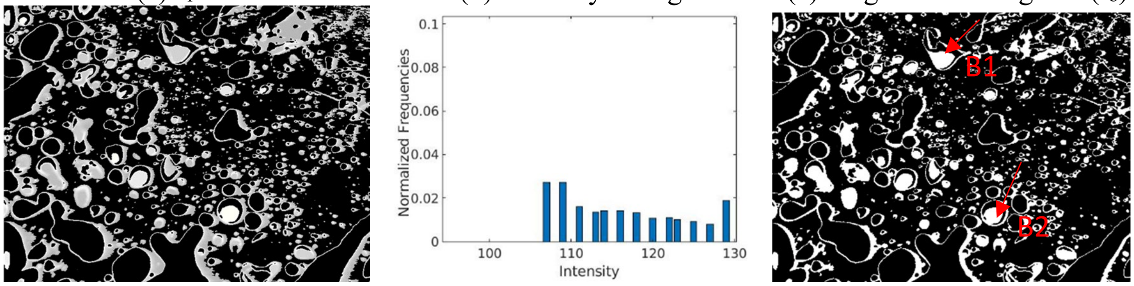

(d) Contrast-enhanced $\mathbf{I}_{\mathbf{nb}}$ (e) Histogram w/o the first peak (f) Dark bubble regions

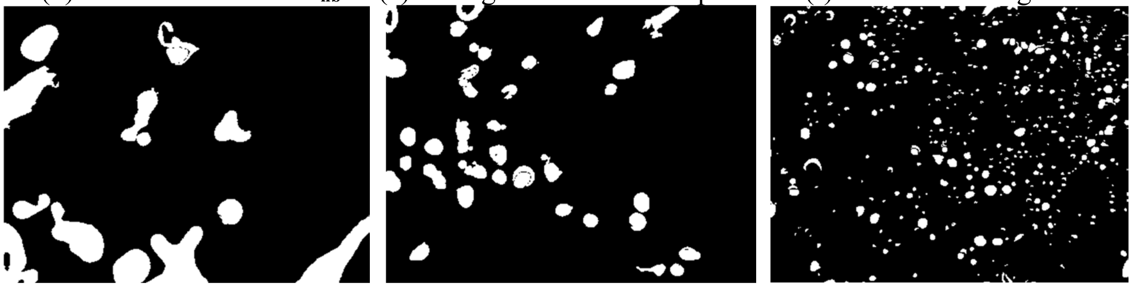

(g) Large bubbles (h) Medium bubbles (i) Small bubbles

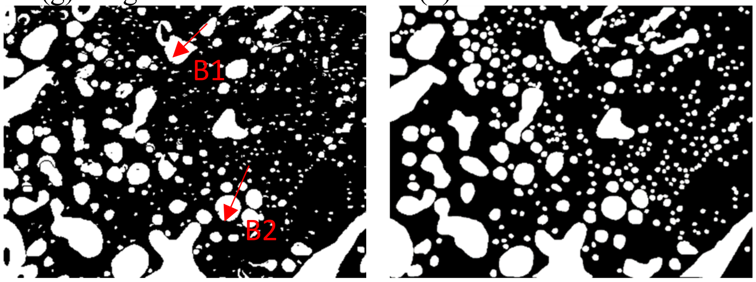

(j) Combined result (k) Manually marked bubbles

Fig. 4. Bubble segmentation using automatic thresholding.

In Fig. 5, the proposed segmentation approach is applied to a new image patch. The first column shows a whole SEM image and its results; and the second column show an image patch (marked in the red rectangle) and the results. Images from rows one to five are the original image, reversed image, bright regions, dark regions, and final segmentation result, respectively.

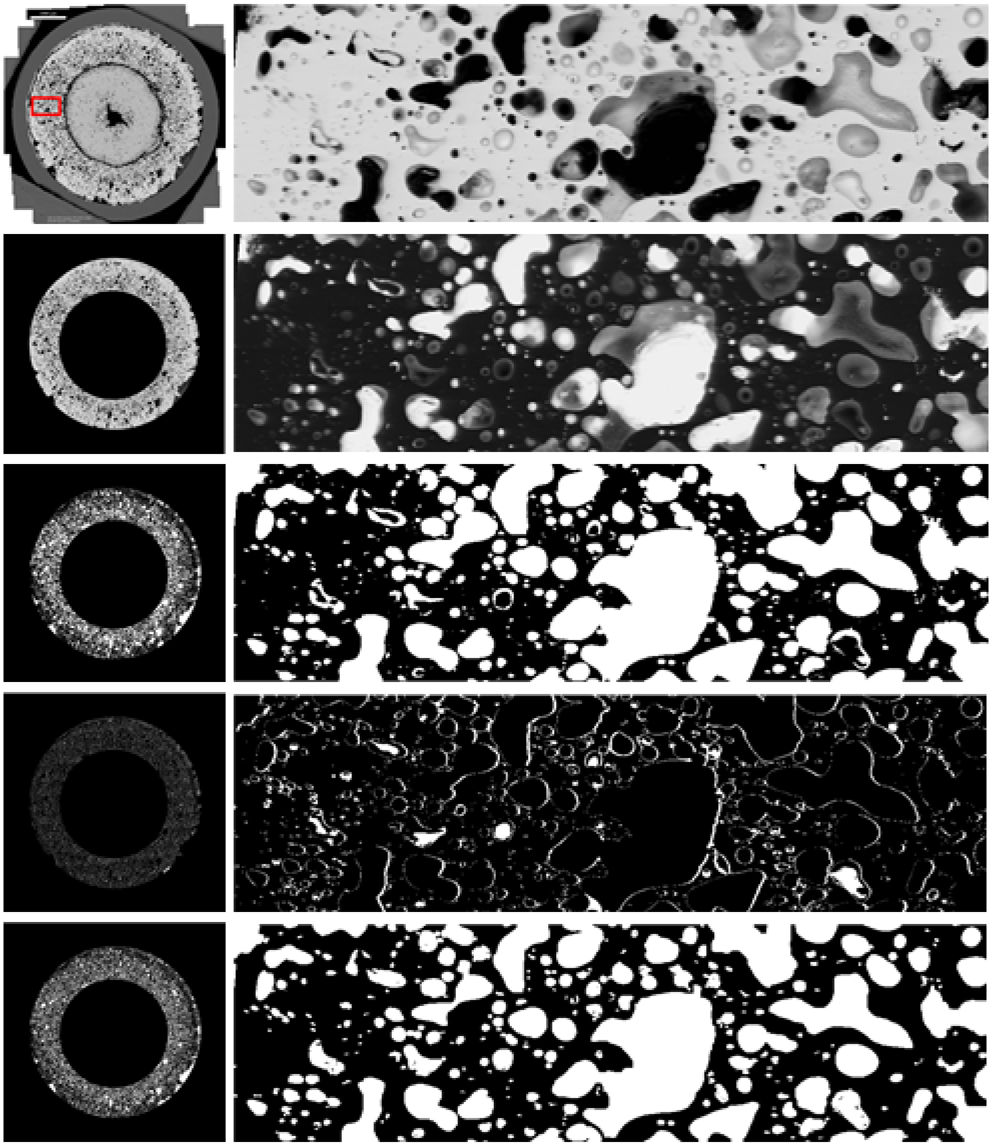

Fig. 5. Bubble segmentation for a whole SEM image.

2.4. Bubble classification using decision tree

All bubbles are classified into three types, connected fission product bubbles ('1'), labelled white color in Fig. 3(c), connected empty bubbles ('2'), labelled blue color in Fig. 3(c), and isolated bubbles ('3'), labelled green color in Fig. 3(c). For each bubble, we extract 18 features including the bubble size (F1), intensity histogram (F2 - F14), mean intensity (F15), intensity standard deviation (F16), intensity range (F17) and the shape convexity (F18) which is defined as the ratio of area over convex area. The features are developed based on the three major observations: (1) Isolated bubbles

usually are smaller than the connected ones, and most of the connected empty bubbles are smaller than the connected bubbles with fission product (F1); (2) connected bubbles have poor roundness (F18); (3) The inner image regions of isolated bubbles are homogeneous, but connected bubble are inhomogeneous (F2-F17). Consequently, the intensity distributions of the three types of bubbles are different from each other. The intensity distribution of an isolated bubble usually has only a single peak, while the connected bubble usually has more than one peak. A decision tree (DT)-based machine learning algorithm is utilized to provide an interpretable bubble classification.

The reasons for choosing DT are as following: 1) although artificial neural networks (ANNs)[13] , especially deep learning (DL)[14], are widely used for classification problems, the approaches have poor interpretability. Meanwhile, DL-based methods need large, high-quality labeled training datasets to guarantee the performance, which might be unavailable in many applications. 2) The Linear Regression[15] approaches are simple to implement and can also interpret the output efficiency. The predefined linear relationship among the features/properties, however, may not suit many problems. 3) DTs can model non-linear relationships and are highly interpretable. During the training process, a DT iteratively splits the feature space by choosing features and cut-points as the thresholds until the stopping criterion is satisfied. The training/splitting process of a typical DT generates a binary tree, i.e., each tree node has two branches. For a given test sample, the decision-making process is to travel the tree from the root to one of the leaves. The process can be explicitly explained using the path the test sample visited. In addition, DTs can explain the importance of each input feature.

A sample binary DT is shown in Fig. 6. Each tree node is associated with a feaure and a cut-point to split the feature space, e.g., the root node applys cut-point value 225.5 to the feature **F1**. Each path from the root to a leaf is a decision-making process using a set of combined conditions. For an instance, the red path classifies a bubble as an isolated bubble (‘3’) if the bubble’s size (**F1**) is less than 225.5 and the convexity (**F18**) is greater than 96.8; if **F1** is greater than 225.5 and the 11th bin of the histogram (**F12**) is less than 7.7, the bubble will be classified as a connected bubble with fission product (‘**1**’); if **F1** is greater than 225.5 and **F12** is greater than 7.7, the bubble will be classified as a connected empty bubble

(‘**2**’). The full train decision tree is shown in Fig. 7. ***As shown in Fig.7, the bubble size is the most efficient feature to classify the isolated bubbles and connected bubbles. Most of the bubbles with lanthanides appear larger size, poorer roundness, and inhomogeneous inner bubble surface. Some bubbles with lanthanides are small size but poor roundness with special F2 – F14 values.*** Meanwhile, the DT model outputs the importance of each feature. As shown in Fig. 8, **F1** is the dominant feature that determins the bubble types, and **F4, F12, F13, F18** are secondary contributors.

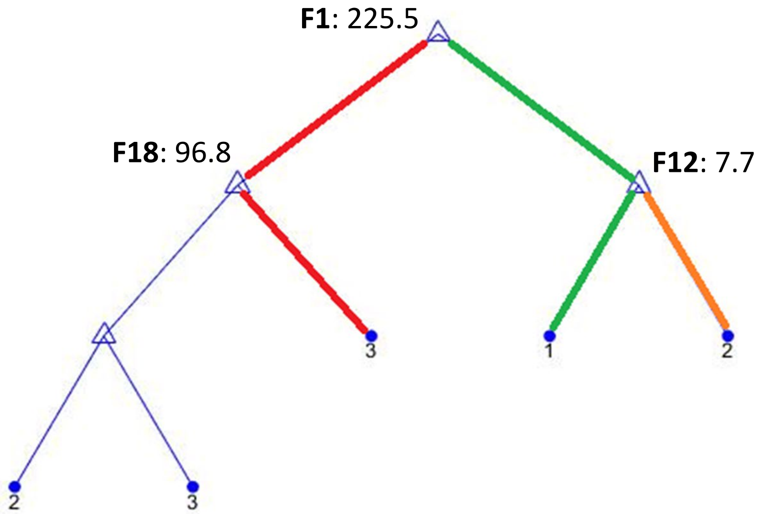

Fig. 6. A Decision Tree classifier.

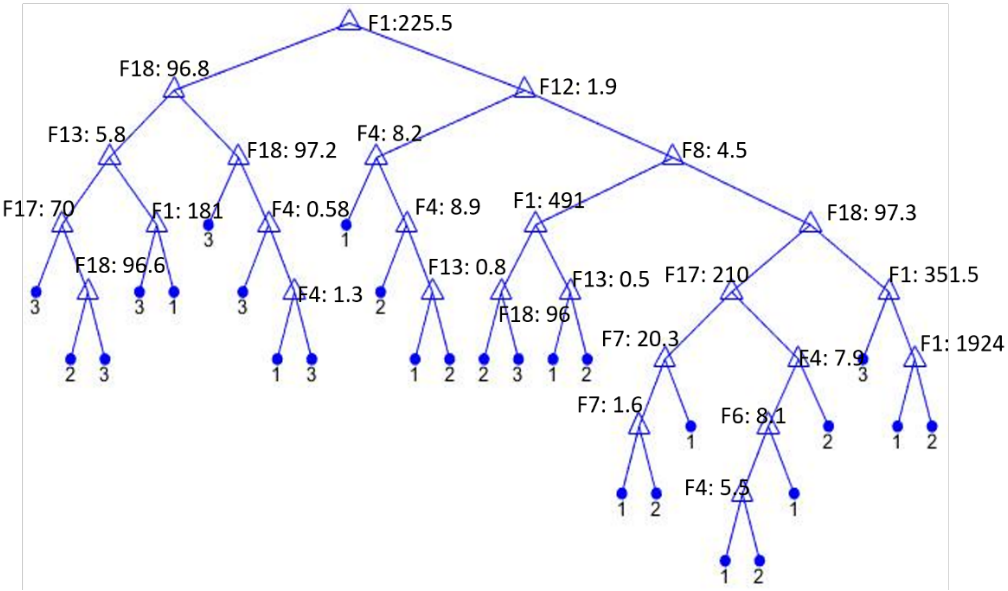

Fig. 7. The full decision tree for bubble classification.

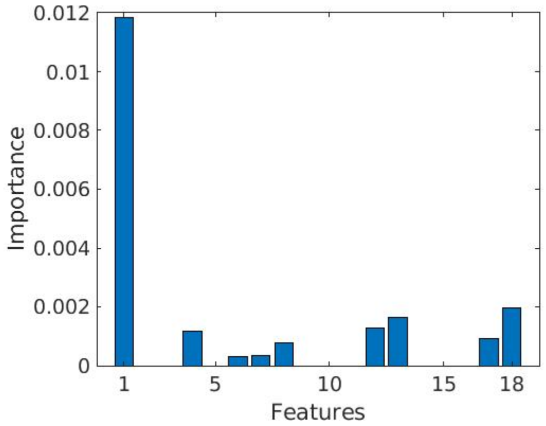

Fig. 8. Quantitative feature importance.

3. Results and Discussion

3.1. Bubble segmentation evaluation

Evaluation of background removal. Since only partial annotated image is available, the ground truth (*GT*) are the pixels which are marked as bubbles. The following metrics are used to evaluate the performance: true positives ratio (*TPR*) and true negative ratio (*TNR*). *TPR* evaluates the ratio that the bubbles in the ground truth are detected as bubbles. *TNR* evaluates the ratio that the bubbles in the ground truth are not detected as bubbles. The metrics are defined as follows:

$$TPR = \frac{|GT \cap A_s|}{|GT|} \tag{3}$$

$$TNR = 1 - TPR \tag{4}$$

where A_s is the segmentation map, and *GT* is the ground truth map. For all the metrics, the values are in [0,1], and the higher value of *TPR* and lower value of *TNR* indicate better performance. Segmentation results of two samples images are shown in Fig. 9. The *TPR* values of Fig.9(a) and Fig.9 (d) are **0.96** and **0.97**, respectively.

Evaluation based bubble detection and segmentation. In the paper, the commonly used metrics, Precision Ratio (PR) and Intersection Over Union (IOU), are utilized to evaluate the performance based on different bubble size level, respectively. IOU is a metric that finds the difference between ground truth annotations and predicted results. Precision ratio is the number of correct detected objects divided by the number of ground truth annotations. For each bubble i in the ground truth notations, we will match it by using the object j in the detection result which has the maximum intersection set with the bubble i. The following criteria will be applied to determine whether the detection is correct or not: 1) bubble i is a small size bubble and the intersection set contains at least 10 pixels; 2) bubble i is a medium size bubble and the intersection set over the number of pixels of ith bubble is over 0.3; 3) bubble i is a large size bubble and the intersection set over the number of pixels of ith bubble is over 0.5. The $IOU(k)$ is calculated by the following equation, where k indicates the small, medium and large bubbles with value 1, 2, 3. The overall performance is listed as Table 1.

$$IOU(k) = \frac{\sum_{bubble\ i \in k} \frac{|bubble(i) \cap bubble(j)|}{|bubble(i) \cup bubble(j)|}}{\sum_{bubble\ i \in k} 1}$$

Table 1. Overall performance.

		Small bubbles (<=50 pixels)	Medium Bubbles (<=500 pixels)	Large Bubbles (> 500 pixels)
Fig.9 (a)	Number of bubbles	8	295	53

	Detected bubbles	6	258	48
	Precisions	0.75	0.87	0.91
	IOU	0.55	0.74	0.77
Fig. 9 (d)	Number of bubbles	19	578	156
	Detected bubbles	16	461	132
	Precision	0.8421	0.7976	0.8462
	IOU	0.4709	0.5865	0.7362

From Fig.9 and Table 1, we found the proposed method obtained better performance on the images with lower bubble density distribution. The reason is that the high bubble density case will cause more unexpected connected bubbles which makes a poor performance on large size bubbles. Additionally, the overall performances on medium and large size bubbles are much better than that on small bubbles. The proposed method ignores the small bubbles with less than 10 pixels, and the morphological erosion operations will cause some small bubbles to be eliminated. Moreover, the detection of bubble boundaries could be improved. In the future, we will annotate more images and make a benchmark ready for other supervised Machine Learning-based approaches.

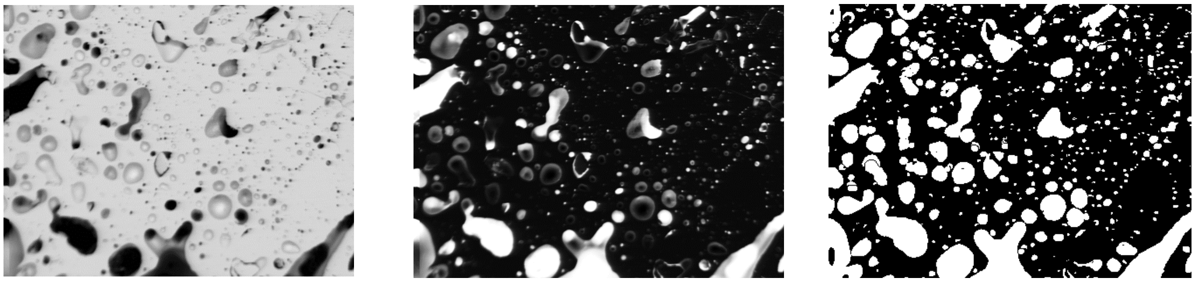

(a) original image 1 (b) background removal result (c) ground truth

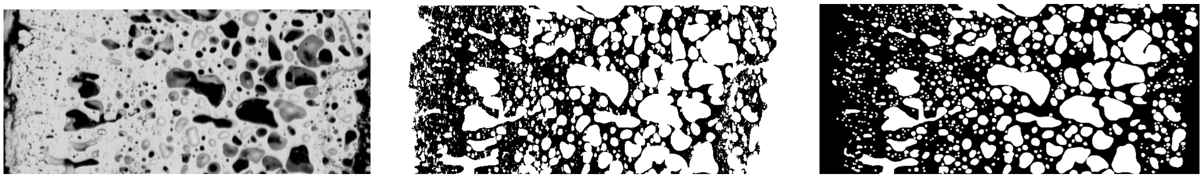

(d) Original image 2 (e) background removal result (f) ground truth

Fig. 9. Background removal result.

3.2. Bubble classification evaluation

To classify the bubble types with a data-drive model, we marked 789 bubbles, in which there are 81 connected with fission product bubbles, 95 connected empty bubbles, and 613 isolated bubbles. We separated the entire dataset into a disjointly training dataset (80% of the whole dataset) and a test dataset (rest of the 20% data). During the training stage, we applied a ten-fold cross-validation technique to create and evaluate the DT model. The advantage of ten-fold cross-validation is that all samples in the training dataset participate in the training stage, and each sample is used for validation exactly once. In other words, every iteration will have 90% and 10% training data as training and validation, respectively. The test stage is to provide an unbiased evaluation of the final model by using the test dataset. The commonly used metrics Accuracy, Precision, Recall and F_measure will be utilized to evaluate the performance[16].

$$Accuracy = \frac{\sum_j answer_j == predict_j}{\sum_j 1}$$

$$Precision = \frac{\sum_j answer_j == predict_j}{\sum_j predict_j == 1}$$

$$Recall = \frac{\sum_j answer_j == predict_j}{\sum_j answer_j == 1}$$

$$F\_measure = \frac{2 * Precision * Recall}{(Precision + Recall\ )}$$

where $answer$ is the bubble label sequence, and $predict$ is the predict result sequence generated by the DT model. For all the metrics, the values are in [0,1], and the higher value of $Accuracy$ and $F\_measure$ indicate better performance. The overall performance is shown in Table 2.

Table 2. Classification evaluation.

	Bubble types	Accuracy	Precision	Recall	F_measure
Test dataset	Connected with fission product bubbles	0.85	0.47	0.29	0.36
	Connected empty bubbles	0.86	0.32	0.32	0.32
	Isolated bubbles	0.89	0.96	0.90	0.93
Entire dataset	Connected with fission product bubbles	0.94	0.69	0.84	0.76
	Connected empty bubbles	0.94	0.75	0.74	0.74
	Isolated bubbles	0.95	0.98	0.96	0.97

Since our training dataset is bias, which has small portion of connected fission product bubbles and connected empty bubbles, but large amount of isolated bubbles, the classification performance on the isolated bubbles is much better than the other bubble classes. To improve the classification performance on the connected bubbles, we will annotate more bubbles and build a benchmark with balanced samples for each type of bubbles. Currently, it's challenge to label the small bubbles' categories manually. ***The expertise look insight the small bubbles in pixel scale to confirm whether the bubble contains fission product. The visual bias exists when the expertise labels the bubbles in pixel scale, especially labelling thousands of bubbles***. In the future, we will utilize the DT model to label the bubble's category if the category is difficult to be determined manually.

3.3. Bubble statistics and its implication on nuclear fuel performance

The effect of fission gas bubbles on nuclear fuel performance have been extensively studied and focused on its effect on fuel swelling[2]. The gaseous fission product atoms have a limited solubility inside fuel matrix and tend to precipitate out in bubble form. Before releasing into plenum or the void space inside fuel rod, the fission gas bubbles grow with burnup as more gaseous fission products are produced by fission reaction. When there is a preexisting bubble nearby, the growing bubble is expected to combine with the neighboring bubble to reduce the bubble surface area and to lower surface energy.

Accurate bubble statistics is the first step to derive the effect of gas bubbles on fuel performance. The bubble statistics of a total of ~19,000 bubbles over an area of 11 mm^2 are shown in Fig. 10-12. Fig.10(a) is an overview of fuel cross section and the illustration of 11 annulus (ring) diagrams in annular α-U region numbered in a sequence with each annular (ring) thickness about 0.08 mm (outer radius – inner radius), from Ring 1 close to the interface of annular α-U region and UZr_{2+x} center region (about 0.84 mm away from the cladding) to Ring 11 next to cold cladding inner surface. Fig.10(b) shows the bubble density (the number of bubbles per unit area) at each of the 11 rings, with three categories of bubble size. For large bubbles (area coverage > 205 μm^2, corresponding to diameter > 16.2 μm of round-shaped bubbles, in which $diameter = 2 \times \sqrt{area/\pi}$), the bubble density stays relatively constant at the distance between 0.84 mm and 0.28 mm from the inner cladding, then decreases almost linearly with decreasing distance towards the inner cladding. For the intermediate bubbles ($32 < area \leq 205\ \mu m^2$ or equivalent $6.4 < diameter \leq 16.2\ \mu m$ of round-shaped bubbles), the bubble density stays relative stable at the distance between 0.84 mm and 0.28 mm from the inner cladding but increases linearly with decreasing distance until 0.12 mm away from inner cladding and decreases slight at the last ring (Ring 11) next to the inner cladding. The small bubble density follows a similar trend as the intermediate bubble density.

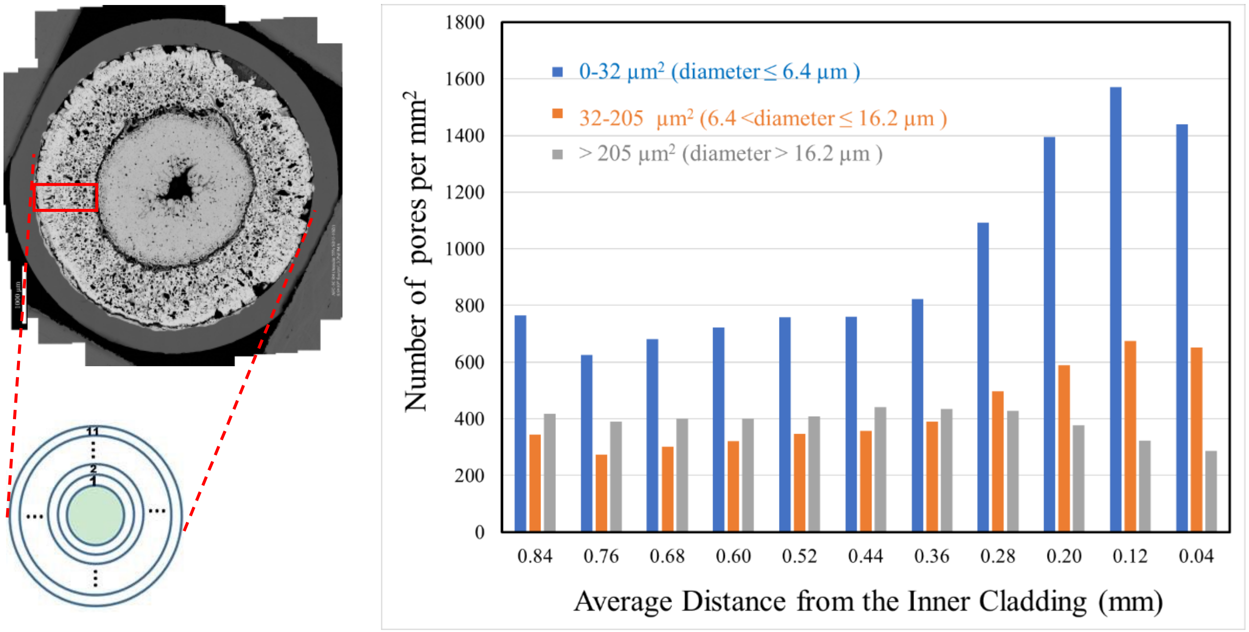

(a) (b)

Fig. 10. (a) overview of fuel cross section and the 11 ring diagrams of α-U region numbered in a sequence. (b) the number of bubbles per unit area (bubble density) at each ring. The x-axis is the average distance of each ring from the inner cladding surface.

Though visually there seems a greater number of bubbles close to cladding, the actual porosity area is much higher close to the fuel center than that close to cladding as shown in Fig.11(a). The ratio of the solid area over the bubble area in Ring 11 (next to the cladding) is about 2.7 times of that in Ring 2, or 3, or 4 (0.6-0.76 mm away from the cladding), as shown in Fig.11(b). The thermal conductivity of the bubbles should be equal to that of the filling gas (helium or fission gas or a mixture of them), which is much smaller than that of α-U (the solid area), so the inhomogeneous degradation of thermal conductivity along the radial direction is revealed by the ratio of each ring zone covered by solid vs bubble in area percentage, with inner rings much lower thermal conductivity and outer rings higher thermal conductivity. Such bubble statistics, which has never been reported before and cannot easily be arrived at without ML models, can be fed into fuel performance code, and make it possible to quantify the inhomogeneous thermal conductivity degradation from fuel center to cladding. ***Note that the heat conduction of nuclear fuel is primarily along the radial direction from the fuel center to the cladding, neglecting the heat conduction in the axial and azimuthal directions.[17] Therefore, the cross-section porosity determines thermal conductivity degradation on the assumption that the cross-section microstructure is representative of the whole fuel pellet. In the future, the 3D microstructure from X-ray tomography as well as focused-ion-beam sectioned images will be investigated to verify the above assumption. Furthermore,*** future work will add physical descriptors[12] based on bubble shapes and orientation to get a better statistic of effective thermal conductivity[18,19] along the radial direction. In addition, local thermal conductivity measurements using TCM will be performed to compare and to calibrate the ML image driven data.

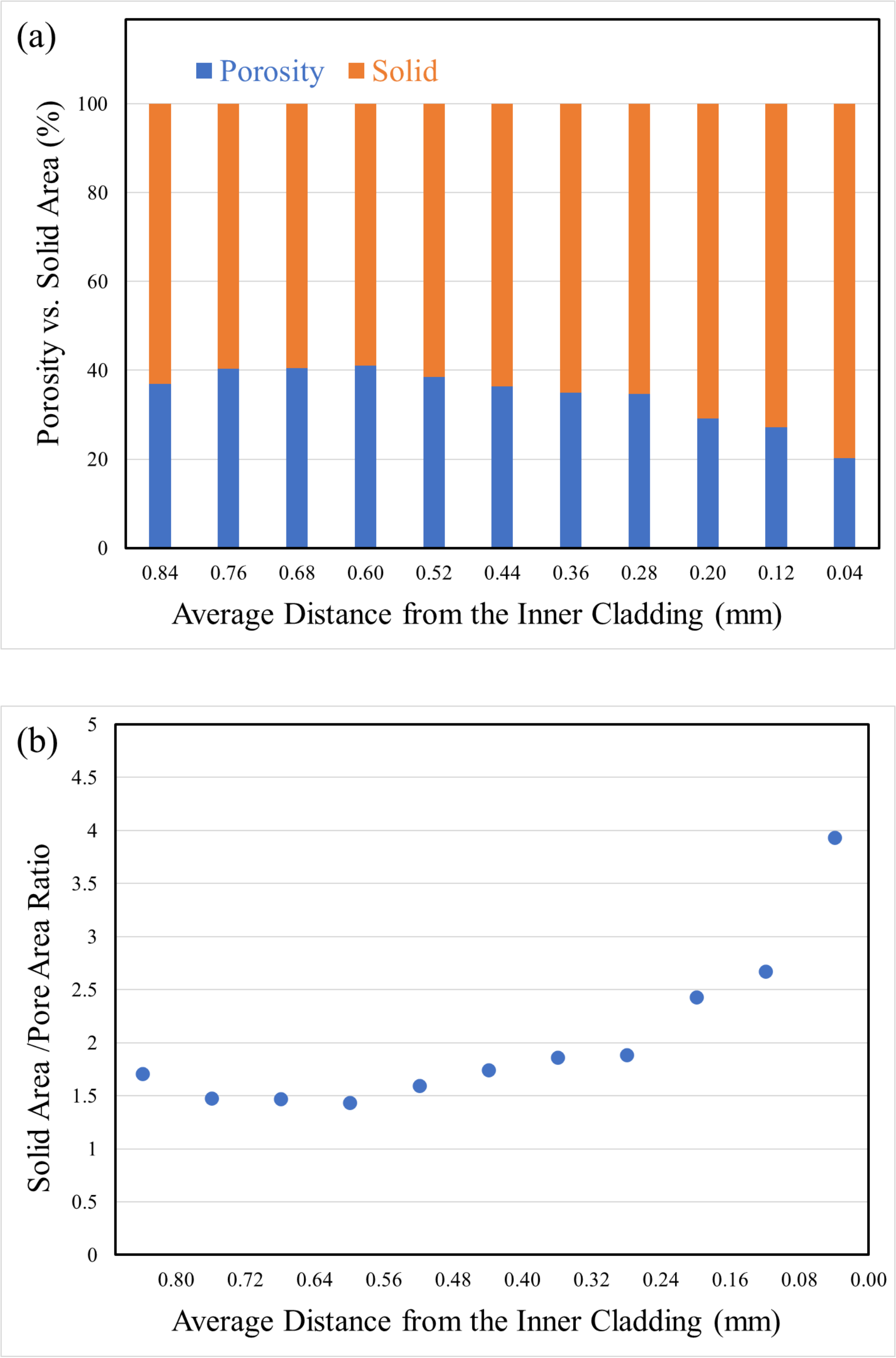

Fig. 11. (a) The percentage of porosity and solid area (b) the ratio of solid area over the pore area at each ring.

Lanthanides, fission products in the fuel, can react with the HT9 cladding and results in the thinning of the cladding wall. Lanthanides move down the temperature gradient along the interconnected bubbles (channel) to the inner cladding surface. As shown in Fig.12(a), bubbles get interconnected due to irradiation and serve as a short path for lanthanides transportation. Not every interconnected bubble has lanthanides as shown in Fig.12(b). It is necessary to train the ML model to distinguish isolated bubbles, connected bubbles, and connected bubbles with/without lanthanides for better understanding of lanthanides migration. As clearly demonstrated in Fig.12(c) and (d), the isolated bubble density (number per mm^2) is much higher at outer rings (up to 0.28 mm away from the cladding) than at inner rings. Out of the connected bubbles, the bubble density with lanthanides stays relative stable up to 0.52 mm away from the cladding and decreases almost linearly from the area of 0.52 mm to 0.84 mm away from the cladding (Fig.12(e)). The connected bubbles close to the center is 5 times more likely to have lanthanides than outer fuel region (Fig.12(f)). How these bubble statistics relate to fuel performance needs further investigation, nevertheless, the ML provides us quantitative data, which are extremely difficult to derive manually, to look into the lanthanide migration and FCCI.

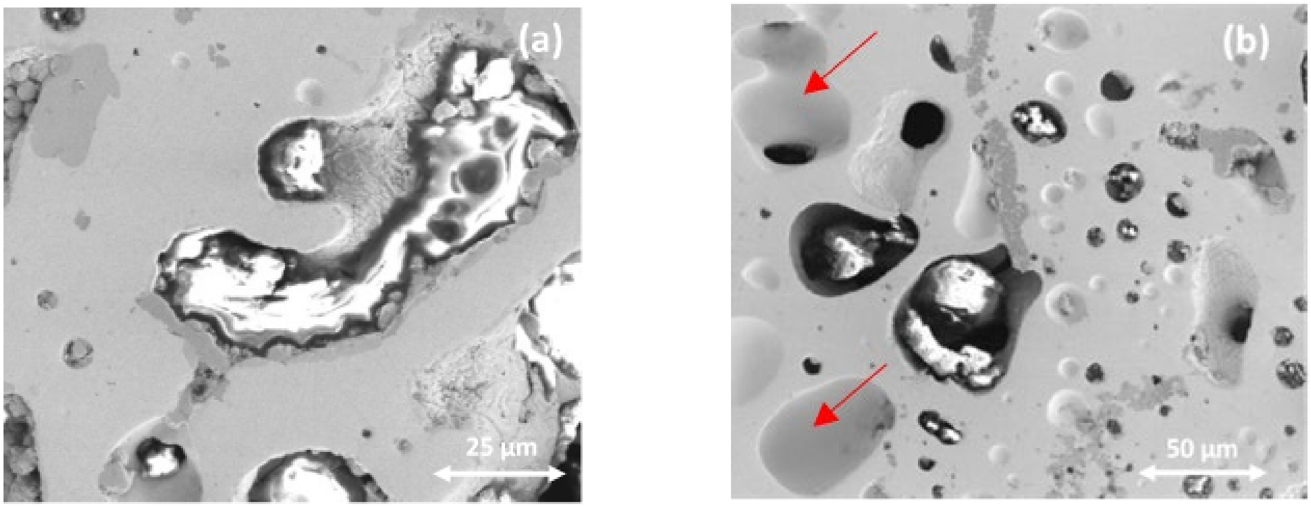

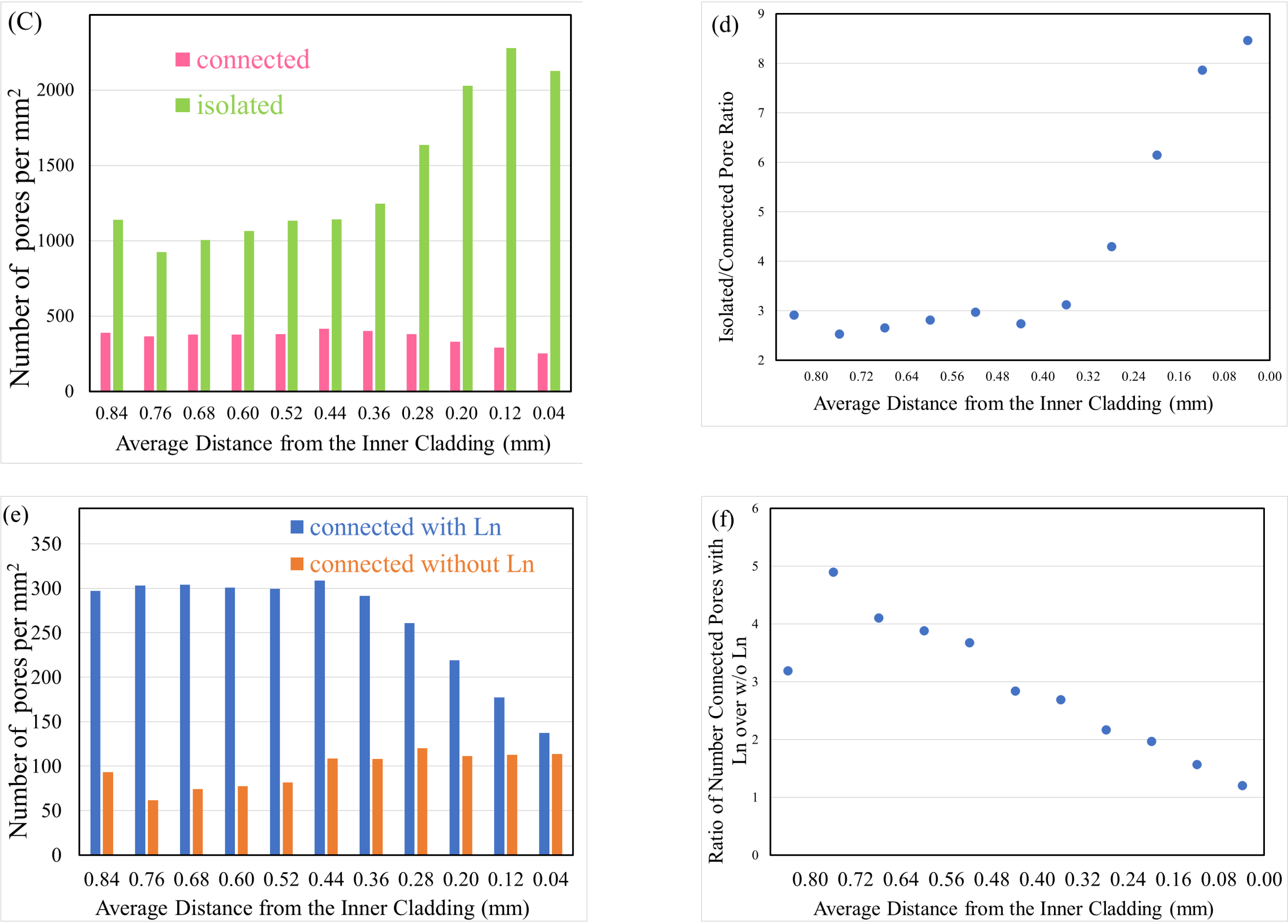

Fig.12. (a) image of connected bubbles with Ln inside, (b) image of connected bubbles do not have lanthanide at all. (highlighted by red arrow), (c) the number of connected and isolated bubbles per mm^2 at each ring, (d) the ratio of number of isolated bubbles over that of connected bubbles at each ring, (e) within the connected bubbles, the bubble density with and without Ln at each ring (f) the ratio of number of bubbles with Ln over that without Ln.

4. Conclusion

This work presents a showcase of a machine learning approach to distinguish/identify the bubble features from microscope images of irradiated metallic uranium fuel. The annular α-U region with area of ~11 mm^2 are split into 11 rings follows in-pile temperature gradient, within which about 19,000 bubbles are studied by machine learning. We are able to derive the bubble statistics and relate the results to fuel performance such as the lanthanide migration and potentially thermal conductivity degradation.

The results are as follows:

1. Temperature favors the growth of fission gas bubble. Regions close to cold cladding is dominated by small pores, while in hot fuel region, there are more large bubbles
2. Due to the large pores in hot region, the area portion ratio of solid vs pore is doubled compared to regions close to cold cladding than hot fuel center.
3. Overall, there are more isolated pores than the connected pores. At hot fuel region, the ratio of the number of isolated pores over the connected pores is 3. The ratio increases to 9 at region close to cold cladding.
4. Among the connected pores, the portion with lanthanide is 5 times of without lanthanide at hot fuel region but linearly decreased to same amount at cold cladding region.

This quantitative data from machine learning will be feed into fuel design code for better prediction of fuel performance.

5. Acknowledgements

The authors acknowledge the support of US Department of energy Advanced Fuel Campaign on the experimental data collection. Insightful discussion with Larry K Aagesen Jr. is also greatly appreciated. This work was supported by the U.S. Department of Energy, Office of Nuclear Energy under DOE Idaho Operations Office Contract DE-AC07-05ID14517. Accordingly, the U.S. Government retains and the publisher, by accepting the article for publication, acknowledges that the U.S. Government retains a nonexclusive, paid-up, irrevocable, worldwide license to publish or reproduce the published form of this manuscript or allow others to do so, for U.S. Government purposes.

6. Disclaimer

Authors have no known competing financial interests.

7. Data availability statement

The data that support the findings of this study are available from the corresponding author upon reasonable request.

8. Reference

1 Janney, D. E. & Hayes, S. L. Experimentally Known Properties of U-10Zr Alloys: A Critical Review. *Nucl Technol* **203**, 109-128, doi:10.1080/00295450.2018.1435137 (2018).

2 Carmack, W. J. *et al.* Metallic fuels for advanced reactors. *J Nucl Mater* **392**, 139-150, doi:10.1016/j.jnucmat.2009.03.007 (2009).

3 Yao, T. K. *et al.* alpha-U and omega-UZr2 in neutron irradiated U-10Zr annular metallic fuel. *J Nucl Mater* **542**, doi:ARTN 152536
10.1016/j.jnucmat.2020.152536 (2020).

4 Benson, M. T. *et al.* Out-of-pile and postirradiated examination of lanthanide and lanthanide-palladium interactions for metallic fuel. *J Nucl Mater* **544**, doi:ARTN 152727
10.1016/j.jnucmat.2020.152727 (2021).

5 Williamson, R. L. *et al.* Multidimensional multiphysics simulation of nuclear fuel behavior. *J Nucl Mater* **423**, 149-163, doi:10.1016/j.jnucmat.2012.01.012 (2012).

6 Keiser, D. D. Fuel cladding chemical interaction in metallic sodium fast reactor fuels: A historical perspective. *J Nucl Mater* **514**, 393-398, doi:10.1016/j.jnucmat.2018.09.045 (2019).

7 Ronchi, C., Sheindlin, M., Staicu, D. & Kinoshita, M. Effect of burn-up on the thermal conductivity of uranium dioxide up to 100.000 MWdt(-1). *J Nucl Mater* **327**, 58-76, doi:10.1016/j.jnucmat.2004.01.018 (2004).

8 Bauer, T. H. & Holland, J. W. In-Pile Measurement of the Thermal-Conductivity of Irradiated Metallic Fuel. *Nucl Technol* **110**, 407-421, doi:Doi 10.13182/Nse110-407 (1995).

9 Yun, D., Yacout, A. M., Stan, M., Bauer, T. H. & Wright, A. E. Simulation of the impact of 3-D porosity distribution in metallic U-10Zr fuels. *J Nucl Mater* **448**, 129-138, doi:10.1016/j.jnucmat.2014.02.002 (2014).

10 Zhang, J. & Taylor, C. Studies of Lanthanide Transport in Metallic Fuel. Report No. 14-6482, (The Ohio State University, 2018).

11 Matthews, C., Unal, C., Galloway, J., Keiser, D. D. & Hayes, S. L. Fuel-Cladding Chemical Interaction in U-Pu-Zr Metallic Fuels: A Critical Review. *Nucl Technol* **198**, 231-259, doi:10.1080/00295450.2017.1323535 (2017).

12 Gonzalez, R. C. & Woods., R. E. *Thresholding. In Digital Image Processing*. 595-611 (Pearson Education, 2002).

13 Kamiński, B., Jakubczyk, M. & Szufel, P. A framework for sensitivity analysis of decision trees. *Central European Journal of Operations Research* **26**, 135-159, doi:10.1007/s10100-017-0479-6 (2018).

14 Hopfield, J. J. Neural networks and physical systems with emergent collective computational abilities. *Proceedings of the National Academy of Sciences* **79**, 2554-2558, doi:10.1073/pnas.79.8.2554 (1982).

15 Hidalgo, B. & Goodman, M. Multivariate or Multivariable Regression? *American Journal of Public Health* **103**, 39-40, doi:10.2105/ajph.2012.300897 (2013).

16 Hossin, M. & Sulaiman, M. N. A review on evaluation metrics for data classification evaluations. *International Journal of Data Mining & Knowledge Management Process* **5** (2015).

17 Ghiaasiaan, S. M., Wassel, A. T., Farr, J. L. & Divakaruni, S. M. Heat conduction in nuclear fuel rods. Nuclear Engineering and Design 85, 89-96, doi:https://doi.org/10.1016/0029-5493(85)90275-4 (1985).

18 Wei, H., Bao, H. & Ruan, X. Machine learning prediction of thermal transport in porous media with physics-based descriptors. *International Journal of Heat and Mass Transfer* **160**, 120176, doi:https://doi.org/10.1016/j.ijheatmasstransfer.2020.120176 (2020).

19 Carson, J. K., Lovatt, S. J., Tanner, D. J. & Cleland, A. C. Thermal conductivity bounds for isotropic, porous materials. *International Journal of Heat and Mass Transfer* **48**, 2150-2158, doi:https://doi.org/10.1016/j.ijheatmasstransfer.2004.12.032 (2005).